Angus Academic Press CCAM 2025
ISSN:3007-9640 DOI: https://doi.org/10.70114/acmsr.2025.2.1.P240

Nonlinear Dynamics Model of DFACS with Two Test Masses for Heliocentric Space Gravitational Wave Detection Mission

Bohan Jiao [1, 2, a], Zhaohui Dang [1, 2, b]

[1] School of Astronautics, Northwestern Polytechnical University, Xi'an 710072, China;

[2] National Key Laboratory of Aerospace Flight Dynamics, Northwestern Polytechnical University, Xi'an 710072, China.

[a] jbh2021260474@mail.nwpu.edu.cn, [b] dangzhaohui@nwpu.edu.cn

Abstract. This paper conducts a comprehensive study on the nonlinear dynamic modeling of the two test masses Drag-Free and Attitude Control System (DFACS) for heliocentric gravitational wave detection missions. First, the composition of DFACS and the modeling assumptions are clarified, key reference frames and their transformation relationships are defined, and an innovative modeling approach based on the formation reference frame is proposed to characterize the geometric constraints among multiple DFACSs. Subsequently, a systemic nonlinear dynamic model is established, encompassing spacecraft relative orbital dynamics, relative attitude dynamics, relative motion and attitude dynamics between spacecraft and test masses, optical assembly rotational dynamics, and the coupled dynamics of spacecraft and test masses. This model provides a comprehensive description of the complex dynamic behavior of DFACS. To validate the model's accuracy, a nonlinear dynamics simulation system was developed, and simulation results confirm the model's precision and applicability. The findings offer model support for the control design, state estimation, and performance optimization of DFACS and provide methodological references for future gravitational wave detection mission modeling efforts.

Keywords: Drag-free; DFACS; Dynamics; Modeling.

1. Introduction

Space-based gravitational wave detection aims to capture gravitational wave signals from the universe to obtain information about astrophysical phenomena. It provides a unique observational method for exploring cosmic evolution, celestial structures, and fundamental physical laws[1]. In recent years, space-based gravitational wave detection missions have become a major focus of international astronomy research, with representative projects including the European Space Agency's (ESA) Laser Interferometer Space Antenna (LISA)[2], China's Taiji[3], and TianQin[4]. These missions rely on ultra-high precision interferometric measurement techniques, requiring detection of distance variations on the order of picometers between spacecraft. In such high-precision detection missions, even the slightest external disturbances—such as solar wind, cosmic dust impacts, or the release of residual gases from the spacecraft—can have significant effects on measurement results. To ensure that the detector can stably and accurately follow the minuscule spacetime distortions induced by gravitational waves, drag-free control technology is indispensable, giving rise to the DFACS.

The dynamic model of DFACS is crucial to the success of space-based gravitational wave detection missions. Dynamic modeling provides the foundation for understanding how detectors move and respond to external disturbances in the complex space environment. An accurate dynamic model not only captures the intrinsic dynamic behavior of the system but also describes the relative motion between the test masses and the spacecraft, the influence of external disturbances, and the nonlinear coupling within the system. Through the dynamic modeling of DFACS, the critical physical processes within the system can be comprehensively understood, providing theoretical support for subsequent control design.[5] Furthermore, dynamic modeling is essential for assessing system stability, response characteristics, and performance limits, thereby offering significant references for robust system analysis. As mission complexity increases, the accuracy of the

ISSN:3007-9640 DOI: https://doi.org/10.70114/acmsr.2025.2.1.P240
dynamic model determines control precision and directly impacts the scientific effectiveness of the entire mission. Thus, research on the dynamic modeling of DFACS serves as the foundation for control design and is key to understanding system dynamics and optimizing mission performance.

Various scholars have proposed solutions to DFACS modeling challenges. While DFACS is primarily employed in space-based gravitational wave detection, it also finds applications in satellite navigation, relativistic effect validation, and Earth gravity field measurement. Consequently, dynamic modeling research has been conducted for DFACS in diverse space missions. Despite the differences in mission objectives, the core focus of DFACS modeling lies in describing the motion of the spacecraft, the test masses, and the interactions between them. Since the test masses are central to DFACS's operational principles, variations in the dynamic models across different DFACS are primarily reflected in the number of test masses and spacecraft platforms involved[5]. Based on these variations, existing research categorizes DFACS into five types[5]: SSSPS[6,7], SSDPS[8,9], DSFS[10], TSFS[11,12], and MSFS[13]. On one hand, the addition of more test masses increases the degrees of freedom, complicating the modeling process. On the other hand, multi-spacecraft platforms require not only modeling the dynamics of individual DFACS but also describing the geometric constraints between different DFACS, which necessitates additional formation dynamics modeling. Moreover, the formation mechanism influences the formation dynamics: for the Taiji mission, the spacecraft are on heliocentric orbits, and the formation is based on relative motion dynamics; for the TianQin mission, the spacecraft are on geocentric orbits, and the formation is based on absolute motion dynamics.

Overall, while decades of research on DFACS have yielded numerous studies on its dynamic modeling, very few publications have focused solely on this topic, particularly in the field of space-based gravitational wave detection. Most existing studies emphasize control-related themes, resulting in limited information on dynamic models. However, it is encouraging that the few studies explicitly addressing dynamic modeling provide detailed insights into the modeling process for heliocentric gravitational wave detection missions, offering critical references for this study. For example, Vidano et al.[14] developed a comprehensive DFACS dynamic model for the LISA mission, featuring a formation reference frame based on inter-spacecraft laser links to describe geometric constraints among different DFACS units. However, this approach has certain limitations. First, determining the formation reference frame requires real-time calculations based on the laser signals received by DFACS, which imposes significant computational demands on onboard systems. Second, the time-varying nature of the laser links introduces temporal variability into the reference frame, making geometric constraints less intuitive and complicating the computation of DFACS control objectives. To address these issues, this paper proposes a novel formation reference frame based on the nominal equilateral triangular formation plane. This new reference frame clarifies the geometric constraints between DFACS units and simplifies the computation of control objectives.

Based on the above analysis, this paper focuses on the nonlinear dynamic modeling of the two test masses DFACS for heliocentric gravitational wave detection missions. Section 1 introduces the research background and current status. Section 2 details the composition of DFACS and specifies the modeling assumptions. Section 3 defines the necessary reference frames, establishes the nonlinear dynamic model of DFACS, and derives the linear dynamic model for the Taiji DFACS. Section 4 develops a nonlinear dynamic simulation system for DFACS and validates the accuracy of the proposed model. Section 5 concludes the study.

2. Plant Description

2.1 The Composition of DFACS

The principle of space-based gravitational wave detection relies on the polarization characteristics of gravitational waves. Freely floating test masses within spacecraft detect the minuscule distance variations caused by passing gravitational waves, which are measured using

ISSN:3007-9640 DOI: https://doi.org/10.70114/acmsr.2025.2.1.P240

high-precision laser interferometry due to the weak intensity of these waves. This requires exceptionally stable spacecraft and accurate attitude pointing control to maintain laser links.

For heliocentric gravitational wave detection, a composite formation system has been designed (Fig. 1). It consists of three spacecraft in an equilateral triangular configuration with arm lengths up to 3 million kilometers. The formation’s virtual center follows Earth's orbital path, leading Earth by a specific distance. The DFACS system, including a spacecraft body, two test masses, and optical assemblies, ensures drag-free control. Test masses housed in sensitive cavities are isolated from non-gravitational forces, maintaining high stability.

At the macroscopic level, the triangular formation orbits along Earth's path with uniform spacecraft distribution, maintaining its geometry during detection. Microscopically, each spacecraft includes test masses, optical assemblies for laser interferometry, and an electrostatic suspension system. Thrusters guide the spacecraft to track one test mass, while the suspension system aligns the second test mass with spacecraft motion.

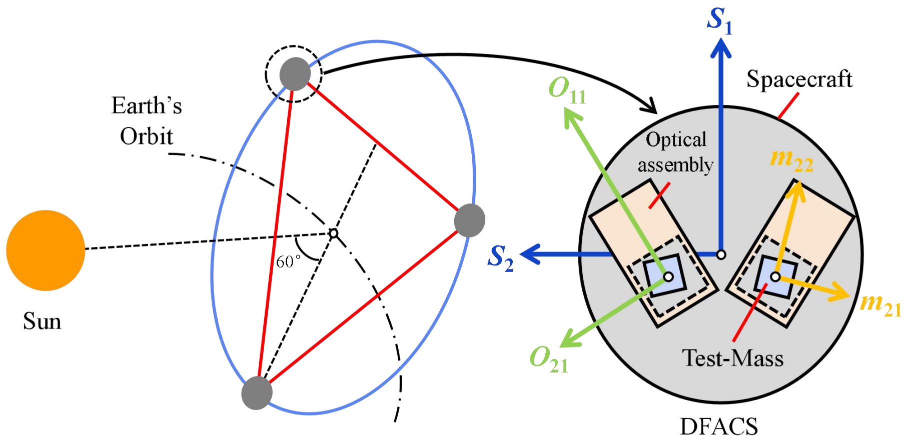

Fig. 1 The composition of heliocentric DFACS with two test masses

2.2 The Assumptions for Dynamic Modeling

For subsequent applications like control and state estimation, a simplified dynamic model retaining key system characteristics is essential. Overly complex models complicate both the modeling process and subsequent tasks. To address this, the following assumptions are made:

Assumption 1. The centers of mass and gravity for both the spacecraft and cubic test masses are assumed to coincide. This simplifies the model by avoiding additional dynamic terms in the Newton-Euler equations.

Assumption 2. Coupling between the spacecraft and test masses is modeled as a second-order spring-damping system, representing residual stiffness and disturbances like gravitational, magnetic, and capacitive sensor interference.

Assumption 3. The small rotational angle (1°) and velocity (10^{-7} rad/s) of the optical assembly are assumed to have negligible impact on spacecraft and test mass dynamics, so coupling terms are omitted.

Assumption 4. The spacecraft and test masses are assumed to experience a two-body gravitational field centered on the Sun, with other celestial influences treated as perturbations.

Assumption 5. The Earth's orbit around the Sun is assumed to be perfectly circular, ignoring perturbing factors on the detection formation.

Assumption 6. The equilateral triangular spacecraft configuration is designed using the Clohessy-Wiltshire (CW) equations.

ISSN:3007-9640 DOI: https://doi.org/10.70114/acmsr.2025.2.1.P240

3. Dynamics Modeling of DFACS with Two Test Masses

3.1 The Coordinate Frames

The relevant coordinate systems used in this paper are defined as follows:

A. The Sun-centered Inertial Reference Frame (IRF): The origin of the Sun-centered inertial reference frame ($\boldsymbol{i}_1,\boldsymbol{i}_2,\boldsymbol{i}_3$) is located at the center of mass of the Sun. The $\boldsymbol{i}_1$ lies in the ecliptic plane and points toward the vernal equinox, the $\boldsymbol{i}_3$ is perpendicular to the ecliptic plane, and the $\boldsymbol{i}_2$ lies in the ecliptic plane, forming a right-handed coordinate system with the $\boldsymbol{i}_1$ and $\boldsymbol{i}_3$ (hereafter referred to as the inertial reference frame for simplicity).

B. The Local Vertical Local Horizontal Reference Frame (LVLH): The LVLH reference frame ($\boldsymbol{L}_1,\boldsymbol{L}_2,\boldsymbol{L}_3$) has its origin at the virtual center of the equilateral triangle formation in the ideal two-body gravitational field. The $\boldsymbol{L}_1$ lies in the ecliptic plane, pointing from the Sun toward the formation's virtual center, the $\boldsymbol{L}_3$ is perpendicular to the ecliptic plane and points in the direction of the formation's angular momentum, and the $\boldsymbol{L}_2$ lies in the ecliptic plane, forming a right-handed coordinate system with the $\boldsymbol{L}_1$ and $\boldsymbol{L}_3$.

C. The Formation Reference Frame (FRF): The formation reference frame ($\boldsymbol{C}_1,\boldsymbol{C}_2,\boldsymbol{C}_3$) has its origin at the virtual center of the equilateral triangle formation in the ideal two-body gravitational field. The $\boldsymbol{C}_1$ lies in the plane of the relative circular orbits and points toward the nominal virtual position of one of the spacecraft, the $\boldsymbol{C}_3$ is perpendicular to the relative orbit plane and points away from the Sun, and the $\boldsymbol{C}_2$ lies in the relative orbit plane, forming a right-handed coordinate system with the $\boldsymbol{C}_1$ and $\boldsymbol{C}_3$.

D. The Spacecraft Reference Frame (SRF): The spacecraft reference frame ($\boldsymbol{S}_1,\boldsymbol{S}_2,\boldsymbol{S}_3$) is centered at the spacecraft's center of mass. The $\boldsymbol{S}_1$ is aligned with the angular bisector of the nominal positions of the two optical assemblys, the $\boldsymbol{S}_3$ is perpendicular to the spacecraft's solar panels (horizontal plane of the spacecraft), and the $\boldsymbol{S}_2$ lies in the horizontal plane of the spacecraft, forming a right-handed coordinate system with the $\boldsymbol{S}_1$ and $\boldsymbol{S}_3$.

E. The Test Mass Reference Frame (MRF): The test mass reference frame ($\boldsymbol{m}_{i1},\boldsymbol{m}_{i2},\boldsymbol{m}_{i3}$, where subscript i denotes the test mass index) is centered at the center of mass of the test mass. The $\boldsymbol{m}_{i1}$ is normal to the test mass surface and points outward along the optical assembly direction, the $\boldsymbol{m}_{i3}$ is normal to the test mass surface and points toward the spacecraft's upper surface, and the $\boldsymbol{m}_{i2}$ is normal to the test mass surface, perpendicular to the $\boldsymbol{m}_{i1}$, and forms a right-handed coordinate system with the $\boldsymbol{m}_{i1}$ and $\boldsymbol{m}_{i3}$.

F. The Optical Assembly Reference Frame (ORF): The optical assembly reference frame ($\boldsymbol{O}_{i1},\boldsymbol{O}_{i2},\boldsymbol{O}_{i3}$, where subscript i denotes the optical assembly index) is centered at the center of the electrostatic suspension system (sensitive cavity). The $\boldsymbol{O}_{i1}$ is aligned with the optical assembly's symmetry axis and points outward along the optical assembly direction, the $\boldsymbol{O}_{i2}$ is perpendicular to the optical assembly's symmetry axis, and the $\boldsymbol{O}_{i3}$ forms a right-handed coordinate system with the $\boldsymbol{O}_{i1}$ and $\boldsymbol{O}_{i2}$.

3.2 Spacecraft Relative Orbital Dynamics

The spacecraft relative orbital dynamics model describes the deviation between the spacecraft's actual position and its nominal position under ideal conditions, forming the basis for formation control. To characterize this deviation, the relative motion dynamics with respect to the ideal formation virtual center are formulated and projected into the FRF.

The spacecraft's relative orbital dynamics model aims to establish the equation for the second derivative of $\boldsymbol{r}_{\mathrm{S}}$. Thus, the core task of the modeling process is to derive the explicit expression for

ISSN:3007-9640 DOI: https://doi.org/10.70114/acmsr.2025.2.1.P240

$\ddot{\boldsymbol{r}}_{\mathrm{S}}$. Since both the linear momentum theorem and the angular momentum theorem describe the dynamics of an object in the inertial frame, it is convenient to perform the derivation using the projection of $\boldsymbol{r}_{\mathrm{S}}$ in the inertial frame, denoted as $\boldsymbol{r}_{\mathrm{S}}^{\mathrm{I}}$. The relationship between $\boldsymbol{r}_{\mathrm{S}}$ and $\boldsymbol{r}_{\mathrm{S}}^{\mathrm{I}}$ can be expressed as:

$$\boldsymbol{r}_{\mathrm{S}}^{\mathrm{I}} = \boldsymbol{T}_{\mathrm{C}}^{\mathrm{I}} \cdot \boldsymbol{r}_{\mathrm{S}} \tag{1}$$

Taking the second derivative of both sides of equation Eq.(1) with respect to time, we obtain:

$$\ddot{\boldsymbol{r}}_{\mathrm{S}} = \boldsymbol{T}_{\mathrm{I}}^{\mathrm{C}} \ddot{\boldsymbol{r}}_{\mathrm{S}}^{\mathrm{I}} - \boldsymbol{\omega}_{\mathrm{P}} \times \boldsymbol{\omega}_{\mathrm{P}} \times \boldsymbol{r}_{\mathrm{S}} - \dot{\boldsymbol{\omega}}_{\mathrm{P}} \times \boldsymbol{r}_{\mathrm{S}} - 2\boldsymbol{\omega}_{\mathrm{P}} \times \dot{\boldsymbol{r}}_{\mathrm{S}} \tag{2}$$

In Eq.(2), $\boldsymbol{T}_{\mathrm{I}}^{\mathrm{C}}$ represents the transformation matrix from FRF to IRF, and $\boldsymbol{\omega}_{\mathrm{P}}$ is the angular velocity vector of FRF relative to IRF, expressed in FRF. By observing Eq.(2), it is evident that $\ddot{\boldsymbol{r}}_{\mathrm{S}}^{\mathrm{I}}$, $\boldsymbol{\omega}_{\mathrm{P}}$, and $\dot{\boldsymbol{\omega}}_{\mathrm{P}}$ are all unknown quantities. Therefore, by determining the specific expressions for these unknowns, the relative orbital dynamics model for the spacecraft can be derived.

For $\boldsymbol{\omega}_{\mathrm{P}}$, which represents the angular velocity of FRF relative to IRF, it can be expanded using kinematic relationships as:

$$\boldsymbol{\omega}_{\mathrm{P}} = \boldsymbol{\omega}_{\mathrm{CL}} + \boldsymbol{T}_{\mathrm{L}}^{\mathrm{C}} \boldsymbol{\omega}_{\mathrm{LI}} \tag{3}$$

where, $\boldsymbol{\omega}_{\mathrm{CL}}$ represents the angular velocity of FRF relative to LVLH coordinate system, expressed in FRF, and $\boldsymbol{\omega}_{\mathrm{LI}}$ represents the angular velocity of LVLH relative to IRF, expressed in LVLH. Based on this, by taking the time derivative of both sides of Eq.(3), the specific expression for $\dot{\boldsymbol{\omega}}_{\mathrm{P}}$ is obtained:

$$\dot{\boldsymbol{\omega}}_{\mathrm{P}} = \dot{\boldsymbol{\omega}}_{\mathrm{CL}} - \boldsymbol{\omega}_{\mathrm{CL}} \times \boldsymbol{T}_{\mathrm{L}}^{\mathrm{C}} \boldsymbol{\omega}_{\mathrm{LI}} + \boldsymbol{T}_{\mathrm{L}}^{\mathrm{C}} \dot{\boldsymbol{\omega}}_{\mathrm{LI}} \tag{4}$$

For $\ddot{\boldsymbol{r}}_{\mathrm{S}}^{\mathrm{I}}$, the detailed expression can be found in Ref.[14]. In summary, the relative orbital dynamics model for the spacecraft is obtained, expressed as:

$$\ddot{\boldsymbol{r}}_{\mathrm{S}} = \boldsymbol{T}_{\mathrm{L}}^{\mathrm{C}} \cdot \left(\mu \frac{\boldsymbol{T}_{\mathrm{I}}^{\mathrm{L}} \boldsymbol{r}_{\mathrm{O}}}{\left| \boldsymbol{T}_{\mathrm{I}}^{\mathrm{L}} \boldsymbol{r}_{\mathrm{O}} \right|^3} - \mu \frac{\boldsymbol{T}_{\mathrm{I}}^{\mathrm{L}} \boldsymbol{r}_{\mathrm{O}} + \boldsymbol{T}_{\mathrm{C}}^{\mathrm{L}} \boldsymbol{r}_{\mathrm{S}}}{\left| \boldsymbol{T}_{\mathrm{I}}^{\mathrm{L}} \boldsymbol{r}_{\mathrm{O}} + \boldsymbol{T}_{\mathrm{C}}^{\mathrm{L}} \boldsymbol{r}_{\mathrm{S}} \right|^3} \right) - \boldsymbol{\omega}_{\mathrm{P}} \times \boldsymbol{\omega}_{\mathrm{P}} \times \boldsymbol{r}_{\mathrm{S}} - \dot{\boldsymbol{\omega}}_{\mathrm{P}} \times \boldsymbol{r}_{\mathrm{S}} - 2\boldsymbol{\omega}_{\mathrm{P}} \times \dot{\boldsymbol{r}}_{\mathrm{S}} + \frac{1}{m_{\mathrm{S}}} \left(\boldsymbol{f}_{\mathrm{SC}}^{\mathrm{T}} + \boldsymbol{f}_{\mathrm{SC}}^{\mathrm{D}} - \boldsymbol{f}_{\mathrm{PM}}^{\mathrm{E}} \right) \tag{5}$$

where, m_{S} is the mass of the spacecraft, $\boldsymbol{f}_{\mathrm{SC}}^{\mathrm{T}}$ and $\boldsymbol{f}_{\mathrm{SC}}^{\mathrm{D}}$ represent the thrust and disturbance forces acting on the spacecraft in IRF, and $\boldsymbol{f}_{\mathrm{SC}}^{\mathrm{E}}$ represents the electrostatic levitation force acting on the test mass, while $-\boldsymbol{f}_{\mathrm{SC}}^{\mathrm{E}}$ represents the reaction force acting on the spacecraft due to the electrostatic levitation.

3.3 Spacecraft relative Attitude Dynamics

The spacecraft attitude dynamics model is established to enable attitude control for constructing inter-satellite laser links. Accordingly, the attitude dynamics model must describe the spacecraft's attitude relative to FRF, ensuring that the attitudes of the three spacecraft with respect to FRF meet the requirements for forming the laser links. This section derives the attitude dynamics of the spacecraft relative to FRF. To simplify the model, the dynamics are projected into SRF.

According to the Newton-Euler equations, the spacecraft attitude dynamics describe the first derivative of the spacecraft angular velocity $\boldsymbol{\omega}_{\mathrm{S}}$. First, based on kinematic relationships, the angular velocity vector of the spacecraft relative to FRF, expressed in SRF, is given by:

$$\boldsymbol{\omega}_{\mathrm{S}} = \boldsymbol{\omega}_{\mathrm{SI}} - \boldsymbol{T}_{\mathrm{C}}^{\mathrm{S}} \boldsymbol{\omega}_{\mathrm{C}} \tag{6}$$

where $\boldsymbol{T}_{\mathrm{C}}^{\mathrm{S}}$ is the transformation matrix from FRF to SRF, $\boldsymbol{\omega}_{\mathrm{SI}}$ represents the inertial angular velocity of the spacecraft projected in SRF, and $\boldsymbol{\omega}_{\mathrm{C}}$ denotes the angular velocity of FRF relative to IRF, projected in FRF. Differentiating both sides of Eq.(6) yields:

$$\dot{\boldsymbol{\omega}}_{\mathrm{S}} = \dot{\boldsymbol{\omega}}_{\mathrm{SI}} + \boldsymbol{\omega}_{\mathrm{S}} \times \boldsymbol{T}_{\mathrm{C}}^{\mathrm{S}} \boldsymbol{\omega}_{\mathrm{C}} - \boldsymbol{T}_{\mathrm{C}}^{\mathrm{S}} \dot{\boldsymbol{\omega}}_{\mathrm{C}} \tag{7}$$

ISSN:3007-9640 DOI: https://doi.org/10.70114/acmsr.2025.2.1.P240

In Eq.(7), $\boldsymbol{\omega}_{\mathrm{C}}$, $\dot{\boldsymbol{\omega}}_{\mathrm{C}}$, and $\dot{\boldsymbol{\omega}}_{\mathrm{SI}}$ are unknowns. By explicitly determining these terms, the attitude dynamics model can be obtained. The detailed expressions of the aforementioned unknown variables are provided in Ref.[14].

In conclusion,, the spacecraft attitude dynamics model is obtained as:

$$\dot{\boldsymbol{\omega}}_{\mathrm{S}} = -\boldsymbol{J}_{\mathrm{S}}^{-1}\left(\boldsymbol{\omega}_{\mathrm{S}} + \boldsymbol{T}_{\mathrm{C}}^{\mathrm{S}}\boldsymbol{\omega}_{\mathrm{C}}\right)\times\boldsymbol{J}_{\mathrm{S}}\left(\boldsymbol{\omega}_{\mathrm{S}} + \boldsymbol{T}_{\mathrm{C}}^{\mathrm{S}}\boldsymbol{\omega}_{\mathrm{C}}\right) + \boldsymbol{\omega}_{\mathrm{S}}\times\boldsymbol{T}_{\mathrm{C}}^{\mathrm{S}}\boldsymbol{\omega}_{\mathrm{C}} - \boldsymbol{T}_{\mathrm{C}}^{\mathrm{S}}\dot{\boldsymbol{\omega}}_{\mathrm{C}} + \boldsymbol{J}_{\mathrm{S}}^{-1}\left(\boldsymbol{M}_{\mathrm{SC}}^{\mathrm{T}} + \boldsymbol{M}_{\mathrm{SC}}^{\mathrm{D}} - \boldsymbol{M}_{\mathrm{PM}}^{\mathrm{E}} + \boldsymbol{M}_{\mathrm{SC}}^{\mathrm{E}} - \boldsymbol{M}_{\mathrm{OA}}^{\mathrm{Couple}}\right) \quad (8)$$

where, $\boldsymbol{J}_{\mathrm{S}}$ is the inertia matrix of the spacecraft, $\boldsymbol{M}_{\mathrm{SC}}^{\mathrm{T}}$ and $\boldsymbol{M}_{\mathrm{SC}}^{\mathrm{D}}$ are the thrust and disturbance torques acting on the spacecraft in SRF, respectively. The term $-\boldsymbol{M}_{\mathrm{OA}}^{\mathrm{Couple}}$ represents the reaction torque induced by the optical assembly 's rotational motion in SRF. The terms $-\boldsymbol{M}_{\mathrm{PM}}^{\mathrm{E}}$ and $\boldsymbol{M}_{\mathrm{SC}}^{\mathrm{E}}$ account for the reaction torque due to electrostatic suspension and the torque induced by the offset between the electrostatic suspension force application point and the spacecraft center of mass in SRF, respectively.

In addition to the attitude dynamics model, an attitude kinematics model is needed to describe the spacecraft's attitude evolution. The quaternion-based attitude kinematics equations are directly given as:

$$\dot{\boldsymbol{q}}_{\mathrm{S}} = \frac{1}{2}\boldsymbol{q}_{\mathrm{S}}\cdot\bar{\boldsymbol{\omega}}_{\mathrm{S}}\,,\ \dot{\boldsymbol{q}}_{\mathrm{SI}} = \frac{1}{2}\boldsymbol{q}_{\mathrm{SI}}\cdot\bar{\boldsymbol{\omega}}_{\mathrm{SI}} \quad (9)$$

where $\boldsymbol{q}_{\mathrm{S}}$ and $\boldsymbol{q}_{\mathrm{SI}}$ represent the spacecraft's quaternion relative to FRF and its inertial quaternion, respectively, and $\bar{\boldsymbol{\omega}}_{\mathrm{S}}$ and $\bar{\boldsymbol{\omega}}_{\mathrm{SI}}$ denote the quaternion representations of the corresponding angular velocity vectors.

3.4 Test Mass Relative Orbital Dynamics

The development of the relative motion dynamics model for the test mass originates from the core concept of drag-free control, aiming to describe the relative positional relationship between the spacecraft and the test mass. Considering the practical scenario, the test mass is housed within a sensitive cavity of the optical assembly, with its relative position measured by sensors mounted on the cavity. Therefore, the dynamics model derived in this section essentially characterizes the relative motion of the test mass with respect to the origin of ORF.

The relative motion dynamics model of the test mass seeks to establish a second-order derivative equation for $\boldsymbol{r}_{\mathrm{M}}$. Following the adopted modeling approach, the relationship between $\boldsymbol{r}_{\mathrm{M}}$ and $\boldsymbol{r}_{\mathrm{M}}^{\mathrm{I}}$ is expressed as follows:

$$\boldsymbol{r}_{\mathrm{M}}^{\mathrm{I}} = \boldsymbol{T}_{\mathrm{O}}^{\mathrm{I}}\cdot\boldsymbol{r}_{\mathrm{M}} \quad (10)$$

Differentiating both sides of Eq.(10) yields:

$$\ddot{\boldsymbol{r}}_{\mathrm{M}} = \boldsymbol{T}_{\mathrm{I}}^{\mathrm{O}}\ddot{\boldsymbol{r}}_{\mathrm{M}}^{\mathrm{I}} - \boldsymbol{\omega}_{\mathrm{O}}\times\boldsymbol{\omega}_{\mathrm{O}}\times\boldsymbol{r}_{\mathrm{M}} - \dot{\boldsymbol{\omega}}_{\mathrm{O}}\times\boldsymbol{r}_{\mathrm{M}} - 2\boldsymbol{\omega}_{\mathrm{O}}\times\dot{\boldsymbol{r}}_{\mathrm{M}} \quad (11)$$

where, $\boldsymbol{T}_{\mathrm{O}}^{\mathrm{I}}$ represents the transformation matrix from ORF to IRF, and $\boldsymbol{\omega}_{\mathrm{O}}$ is the angular velocity of ORF with respect to IRF, projected onto ORF. Observing Eq.(11), it is evident that $\boldsymbol{\omega}_{\mathrm{O}}$, $\dot{\boldsymbol{\omega}}_{\mathrm{O}}$, and $\ddot{\boldsymbol{r}}_{\mathrm{M}}^{\mathrm{I}}$ are all unknown. Therefore, determining the specific expressions of these unknown quantities is essential for deriving the relative orbital dynamics model of the spacecraft. The detailed expressions of the aforementioned unknown variables are provided in Ref.[14].

In summary, the complete relative motion dynamics model for test mass is obtained:

ISSN:3007-9640 DOI: https://doi.org/10.70114/acmsr.2025.2.1.P240

$$\begin{aligned}\ddot{\boldsymbol{r}}_{\mathrm{M}} = \boldsymbol{T}_{\mathrm{I}}^{\mathrm{O}} \Bigg[& -\mu \frac{\boldsymbol{r}_0 + \boldsymbol{T}_{\mathrm{C}}^{\mathrm{I}}\boldsymbol{r}_{\mathrm{S}} + \boldsymbol{T}_{\mathrm{O}}^{\mathrm{I}}\boldsymbol{r}_{\mathrm{M}} + \boldsymbol{T}_{\mathrm{S}}^{\mathrm{I}}\boldsymbol{b}_{\mathrm{S}} + \boldsymbol{T}_{\mathrm{O}}^{\mathrm{I}}\boldsymbol{b}_{\mathrm{M}}}{\left|\boldsymbol{r}_0 + \boldsymbol{T}_{\mathrm{C}}^{\mathrm{I}}\boldsymbol{r}_{\mathrm{S}} + \boldsymbol{T}_{\mathrm{O}}^{\mathrm{I}}\boldsymbol{r}_{\mathrm{M}} + \boldsymbol{T}_{\mathrm{S}}^{\mathrm{I}}\boldsymbol{b}_{\mathrm{S}} + \boldsymbol{T}_{\mathrm{O}}^{\mathrm{I}}\boldsymbol{b}_{\mathrm{M}}\right|^3} + \mu \frac{\boldsymbol{r}_0 + \boldsymbol{T}_{\mathrm{C}}^{\mathrm{I}}\boldsymbol{r}_{\mathrm{S}}}{\left|\boldsymbol{r}_0 + \boldsymbol{T}_{\mathrm{C}}^{\mathrm{I}}\boldsymbol{r}_{\mathrm{S}}\right|^3} \\ & + \frac{1}{m_{\mathrm{M}}}\left(\boldsymbol{f}_{\mathrm{PM}}^{\mathrm{E}} + \boldsymbol{f}_{\mathrm{PM}}^{\mathrm{D}} + \boldsymbol{f}_{\mathrm{PM}}^{\mathrm{SC}}\right) - \frac{1}{m_{\mathrm{S}}}\left(\boldsymbol{f}_{\mathrm{SC}}^{\mathrm{T}} + \boldsymbol{f}_{\mathrm{SC}}^{\mathrm{D}} - \boldsymbol{f}_{\mathrm{PM}}^{\mathrm{E}}\right) \\ & - \left(\boldsymbol{T}_{\mathrm{S}}^{\mathrm{I}}\boldsymbol{\omega}_{\mathrm{SI}} \times \boldsymbol{\omega}_{\mathrm{SI}} + \boldsymbol{T}_{\mathrm{S}}^{\mathrm{I}}\dot{\boldsymbol{\omega}}_{\mathrm{SI}}\right) \times \boldsymbol{b}_{\mathrm{S}} - \left(\boldsymbol{T}_{\mathrm{O}}^{\mathrm{I}}\boldsymbol{\omega}_{\mathrm{O}} \times \boldsymbol{\omega}_{\mathrm{O}} + \boldsymbol{T}_{\mathrm{O}}^{\mathrm{I}}\dot{\boldsymbol{\omega}}_{\mathrm{O}}\right) \times \boldsymbol{b}_{\mathrm{M}} \Bigg] \\ & - \boldsymbol{\omega}_{\mathrm{O}} \times \boldsymbol{\omega}_{\mathrm{O}} \times \boldsymbol{r}_{\mathrm{M}} - \dot{\boldsymbol{\omega}}_{\mathrm{O}} \times \boldsymbol{r}_{\mathrm{M}} - 2\boldsymbol{\omega}_{\mathrm{O}} \times \dot{\boldsymbol{r}}_{\mathrm{M}} \end{aligned} \tag{12}$$

where, m_{M} denotes the mass of the test mass, $\boldsymbol{f}_{\mathrm{PM}}^{\mathrm{E}}$ and $\boldsymbol{f}_{\mathrm{PM}}^{\mathrm{D}}$ are the electrostatic suspension force and disturbance force acting on the test mass in IRF, respectively, and $\boldsymbol{f}_{\mathrm{PM}}^{\mathrm{SC}}$ represents the coupling force between the spacecraft and the test mass in IRF, the angular velocities $\boldsymbol{\omega}_{\mathrm{SI}}$ and $\boldsymbol{\omega}_{\mathrm{O}}$ should be expressed as functions of the relative states $\boldsymbol{\omega}_{\gamma}$ and $\boldsymbol{\omega}_{\mathrm{S}}$:

$$\begin{cases} \boldsymbol{\omega}_{\mathrm{SI}} = \boldsymbol{\omega}_{\mathrm{S}} + \boldsymbol{T}_{\mathrm{C}}^{\mathrm{S}}\boldsymbol{\omega}_{\mathrm{C}} \\ \boldsymbol{\omega}_{\mathrm{O}} = \boldsymbol{\omega}_{\gamma} + \boldsymbol{T}_{\mathrm{S}}^{\mathrm{O}}\boldsymbol{\omega}_{\mathrm{S}} + \boldsymbol{T}_{\mathrm{C}}^{\mathrm{O}}\boldsymbol{\omega}_{\mathrm{C}} \end{cases} \tag{13}$$

3.5 Test Mass Relative Attitude Dynamics

Similar to the relative orbital dynamics model of the test mass, the primary objective of establishing the relative attitude dynamics model of the test mass is to characterize the relative attitude relationship between the spacecraft and the test mass. Fundamentally, this involves deriving the relative attitude dynamics of the test mass with respect to the origin of ORF.

Firstly, based on the kinematic relationships, the angular velocity vector of the test mass relative to ORF, expressed in ORF, is given by:

$$\boldsymbol{\omega}_{\mathrm{M}} = \boldsymbol{\omega}_{\mathrm{MI}} - \boldsymbol{T}_{\mathrm{O}}^{\mathrm{M}}\boldsymbol{\omega}_{\gamma} - \boldsymbol{T}_{\mathrm{S}}^{\mathrm{M}}\boldsymbol{\omega}_{\mathrm{SI}} \tag{14}$$

where $\boldsymbol{T}_{\mathrm{S}}^{\mathrm{M}}$ denotes the transformation matrix from the spacecraft coordinate system to the test mass coordinate system, $\boldsymbol{\omega}_{\mathrm{MI}}$ represents the angular velocity of the test mass relative to IRF projected in MRF, and $\boldsymbol{\omega}_{\gamma}$ denotes the angular velocity of the optical assembly relative to the spacecraft projected in ORF. By differentiating both sides of Eq. (14) with respect to time, the following expression can be obtained:

$$\dot{\boldsymbol{\omega}}_{\mathrm{M}} = \dot{\boldsymbol{\omega}}_{\mathrm{MI}} + \boldsymbol{\omega}_{\mathrm{M}} \times \boldsymbol{T}_{\mathrm{O}}^{\mathrm{M}}\boldsymbol{\omega}_{\gamma} - \boldsymbol{T}_{\mathrm{O}}^{\mathrm{M}}\dot{\boldsymbol{\omega}}_{\gamma} + \boldsymbol{\omega}_{\mathrm{M}} \times \boldsymbol{T}_{\mathrm{S}}^{\mathrm{M}}\boldsymbol{\omega}_{\mathrm{SI}} - \boldsymbol{T}_{\mathrm{S}}^{\mathrm{M}}\dot{\boldsymbol{\omega}}_{\mathrm{SI}} \tag{15}$$

From Eq. (15), it is evident that the quantities $\dot{\boldsymbol{\omega}}_{\mathrm{MI}}$, $\dot{\boldsymbol{\omega}}_{\gamma}$, and $\boldsymbol{\omega}_{\gamma}$ are all unknown. Hence, the explicit expressions for these quantities must be determined to establish the relative attitude dynamics model of the test mass. The detailed expressions of the aforementioned unknown variables are provided in Ref.[14].

In conclusion, the relative attitude dynamics model of the test mass can be obtained:

$$\begin{aligned}\dot{\boldsymbol{\omega}}_{\mathrm{M}} = & \left[-\boldsymbol{J}_{\mathrm{M}}^{-1}\left(\boldsymbol{\omega}_{\mathrm{M}} + \boldsymbol{T}_{\mathrm{O}}^{\mathrm{M}}\boldsymbol{\omega}_{\gamma} + \boldsymbol{T}_{\mathrm{S}}^{\mathrm{M}}\boldsymbol{\omega}_{\mathrm{SI}}\right) \times \boldsymbol{J}_{\mathrm{M}}\left(\boldsymbol{\omega}_{\mathrm{M}} + \boldsymbol{T}_{\mathrm{O}}^{\mathrm{M}}\boldsymbol{\omega}_{\gamma} + \boldsymbol{T}_{\mathrm{S}}^{\mathrm{M}}\boldsymbol{\omega}_{\mathrm{SI}}\right)\right] \\ & - \boldsymbol{T}_{\mathrm{S}}^{\mathrm{M}}\left[-\boldsymbol{J}_{\mathrm{S}}^{-1}\boldsymbol{\omega}_{\mathrm{SI}} \times \boldsymbol{J}_{\mathrm{S}}\boldsymbol{\omega}_{\mathrm{SI}} + \boldsymbol{J}_{\mathrm{S}}^{-1}\left(\boldsymbol{M}_{\mathrm{SC}}^{\mathrm{T}} + \boldsymbol{M}_{\mathrm{SC}}^{\mathrm{D}} - \boldsymbol{M}_{\mathrm{OA}}^{\mathrm{Couple}} - \boldsymbol{M}_{\mathrm{PM}}^{\mathrm{E}} - \boldsymbol{M}_{\mathrm{PM}}^{\mathrm{E}\,\prime}\right)\right] \\ & + \boldsymbol{\omega}_{\mathrm{M}} \times \boldsymbol{T}_{\mathrm{O}}^{\mathrm{M}}\boldsymbol{\omega}_{\gamma} - \boldsymbol{T}_{\mathrm{O}}^{\mathrm{M}}\dot{\boldsymbol{\omega}}_{\gamma} + \boldsymbol{\omega}_{\mathrm{M}} \times \boldsymbol{T}_{\mathrm{S}}^{\mathrm{M}}\boldsymbol{\omega}_{\mathrm{SI}} + \boldsymbol{J}_{\mathrm{M}}^{-1}\left(\boldsymbol{M}_{\mathrm{PM}}^{\mathrm{E}} + \boldsymbol{M}_{\mathrm{PM}}^{\mathrm{D}} + \boldsymbol{M}_{\mathrm{PM}}^{\mathrm{SC}}\right)\end{aligned} \tag{16}$$

where, $\boldsymbol{M}_{\mathrm{PM}}^{\mathrm{E}}$ and $\boldsymbol{M}_{\mathrm{PM}}^{\mathrm{D}}$ represent the electrostatic suspension torque and disturbance torque acting on the test mass in MRF, respectively. $\boldsymbol{M}_{\mathrm{PM}}^{\mathrm{SC}}$ denotes the coupling torque between the spacecraft and the test mass in MRF, $\boldsymbol{\omega}_{\mathrm{SI}}$ should be rewritten according to the form provided in Eq.(13).

ISSN:3007-9640 DOI: https://doi.org/10.70114/acmsr.2025.2.1.P240

3.6 Optical Assembly Rotational Dynamics

The optical assembly rotational dynamics model is primarily used to describe the optical assembly's one-degree-of-freedom rotational motion, specifically deriving the first derivative expression for the angular velocity $\boldsymbol{\omega}_\gamma$ of the optical assembly relative to the spacecraft in ORF. First, the kinematic relationship for $\boldsymbol{\omega}_\gamma$ is given as:

$$\boldsymbol{\omega}_{\mathrm{OI}} = \boldsymbol{\omega}_\gamma + \boldsymbol{T}_{\mathrm{S}}^{\mathrm{O}}\boldsymbol{\omega}_{\mathrm{SI}} = \boldsymbol{\omega}_\zeta + \boldsymbol{T}_{\mathrm{S}}^{\mathrm{O}}\boldsymbol{\omega}_{\mathrm{SI}} \tag{17}$$

where $\boldsymbol{\omega}_{\mathrm{OI}}$ represents the angular velocity of the optical assembly relative to IRF projected in ORF, and $\boldsymbol{\omega}_\zeta$ is the angular velocity of the optical assembly relative to the nominal position, projected in ORF (since the angle between the nominal position and the spacecraft is fixed, $\boldsymbol{\omega}_\gamma = \boldsymbol{\omega}_\zeta$). By further differentiating both sides of Eq.(17), we obtain:

$$\dot{\boldsymbol{\omega}}_\gamma = \dot{\boldsymbol{\omega}}_\zeta = \dot{\boldsymbol{\omega}}_{\mathrm{OI}} + \boldsymbol{\omega}_\zeta \times \boldsymbol{T}_{\mathrm{S}}^{\mathrm{O}}\boldsymbol{\omega}_{\mathrm{SI}} - \boldsymbol{T}_{\mathrm{S}}^{\mathrm{O}}\dot{\boldsymbol{\omega}}_{\mathrm{SI}} \tag{18}$$

From Eq.(18), we observe that $\dot{\boldsymbol{\omega}}_{\mathrm{OI}}$ is an unknown quantity. Therefore, by determining the specific expression for $\dot{\boldsymbol{\omega}}_{\mathrm{OI}}$, the optical assembly rotational dynamics can be derived.

For $\dot{\boldsymbol{\omega}}_{\mathrm{OI}}$, the Newton-Euler equation can be used to obtain:

$$\dot{\boldsymbol{\omega}}_{\mathrm{OI}} = -\boldsymbol{J}_{\mathrm{OA}}^{-1}\boldsymbol{\omega}_{\mathrm{OI}} \times \boldsymbol{J}_{\mathrm{OA}}\boldsymbol{\omega}_{\mathrm{OI}} + \boldsymbol{J}_{\mathrm{OA}}^{-1} \cdot \left(\boldsymbol{M}_{\mathrm{OA}}^{\mathrm{T}} + \boldsymbol{M}_{\mathrm{OA}}^{\mathrm{D}} - \boldsymbol{T}_{\mathrm{M}}^{\mathrm{O}}\boldsymbol{M}_{\mathrm{PM}}^{\mathrm{E}} + \boldsymbol{M}_{\mathrm{OA}}^{\mathrm{E}} + \boldsymbol{M}_{\mathrm{OA}}^{\mathrm{Couple}}\right) \tag{19}$$

where $\boldsymbol{J}_{\mathrm{OA}}$ represents the moment of inertia of the optical assembly about the pivot point, $\boldsymbol{M}_{\mathrm{OA}}^{\mathrm{T}}$ represents the active control torque generated by the motor in ORF, $-\boldsymbol{M}_{\mathrm{PM}}^{\mathrm{E}}$ represents the reaction torque of the electrostatic suspension in MRF, $\boldsymbol{M}_{\mathrm{OA}}^{\mathrm{D}}$ represents the disturbance torque acting on the optical assembly in ORF, and $\boldsymbol{M}_{\mathrm{OA}}^{\mathrm{Couple}}$ represents the torque between the pivot and the optical assembly in ORF.

In summary, the optical assembly rotational dynamics model can be expressed as:

$$\dot{\boldsymbol{\omega}}_\zeta = \boldsymbol{\omega}_\zeta \times \boldsymbol{T}_{\mathrm{S}}^{\mathrm{O}}\boldsymbol{\omega}_{\mathrm{SI}} - \boldsymbol{T}_{\mathrm{S}}^{\mathrm{O}}\dot{\boldsymbol{\omega}}_{\mathrm{SI}} - \boldsymbol{J}_{\mathrm{OA}}^{-1}\boldsymbol{\omega}_{\mathrm{OI}} \times \boldsymbol{J}_{\mathrm{OA}}\boldsymbol{\omega}_{\mathrm{OI}} + \boldsymbol{J}_{\mathrm{OA}}^{-1} \cdot \left(\boldsymbol{M}_{\mathrm{OA}}^{\mathrm{T}} + \boldsymbol{M}_{\mathrm{OA}}^{\mathrm{D}} - \boldsymbol{T}_{\mathrm{M}}^{\mathrm{O}}\boldsymbol{M}_{\mathrm{PM}}^{\mathrm{E}} + \boldsymbol{M}_{\mathrm{OA}}^{\mathrm{E}} + \boldsymbol{M}_{\mathrm{OA}}^{\mathrm{Couple}}\right) \tag{20}$$

where, $\boldsymbol{\omega}_{\mathrm{SI}}$ should be rewritten in the form given in Eq.(13).

3.7 Spacecraft/Test Mass Coupling Dynamics

According to Assumption 2 in Section 2.2, the coupled model of the spacecraft and the test mass is directly expressed as follows:

$$\begin{bmatrix} \boldsymbol{F}_{\mathrm{St}} \\ \boldsymbol{M}_{\mathrm{St}} \end{bmatrix} = \begin{bmatrix} S_{\mathrm{TT}} & S_{\mathrm{RT}} & D_{\mathrm{TT}} & 0 \\ S_{\mathrm{TR}} & S_{\mathrm{RR}} & 0 & D_{\mathrm{RR}} \end{bmatrix} \begin{bmatrix} \boldsymbol{r}_{\mathrm{M}} & \boldsymbol{\theta}_{\mathrm{M}} & \dot{\boldsymbol{r}}_{\mathrm{M}} & \dot{\boldsymbol{\theta}}_{\mathrm{M}} \end{bmatrix}^{\mathrm{T}} \tag{21}$$

where, $\boldsymbol{F}_{\mathrm{St}}$ and $\boldsymbol{M}_{\mathrm{St}}$ represent the coupling force and coupling torque, respectively, between the spacecraft and the test mass in ORF. $\boldsymbol{r}_{\mathrm{M}}$ and $\dot{\boldsymbol{r}}_{\mathrm{M}}$ denote the position and velocity of the test mass relative to the origin of ORF, respectively. Similarly, $\boldsymbol{\theta}_{\mathrm{M}}$ and $\dot{\boldsymbol{\theta}}_{\mathrm{M}}$ denote the orientation and angular velocity of the test mass relative to the origin of ORF. The coefficients S_{TT}, S_{RT}, S_{TR}, and S_{RR} are the stiffness coefficients, while D_{TT} and D_{RR} are the damping coefficients.

4. Dynamic Simulation System of DFACS

Space-based gravitational wave detection requires precise suppression of non-gravitational disturbances via drag-free control, ensuring nearly perfect inertial motion of test masses. This depends on accurate dynamic modeling and robust control design, highlighting the importance of a dynamic simulation system for the DFACS. Such a system enables analysis of complex dynamics, optimization of control strategies, performance validation under disturbances, and support for mission design. This section develops a simulation system for the heliocentric DFACS configuration with dual test masses, based on prior concepts.

ISSN:3007-9640 DOI: https://doi.org/10.70114/acmsr.2025.2.1.P240

4.1 The Composition of the Simulation System

As shown in Fig. 2, the dynamic simulation system comprises four main components: the force/torque computation module, the absolute dynamics propagation module, the relative dynamics computation module, and the relative dynamics propagation module. The functions of each module are described below:

(1) The System Driver Main Program is responsible for managing tasks such as simulation parameter adjustment, system state initialization, parameter injection, and execution settings.

(2) The Force/Torque Computation Module calculates control and disturbance forces acting on the spacecraft, test masses, and optical assemblies. Additionally, it determines coupling forces between the spacecraft and the test masses based on their relative states, as defined in model (21). This module also provides extensible interfaces for integrating advanced force and torque models.

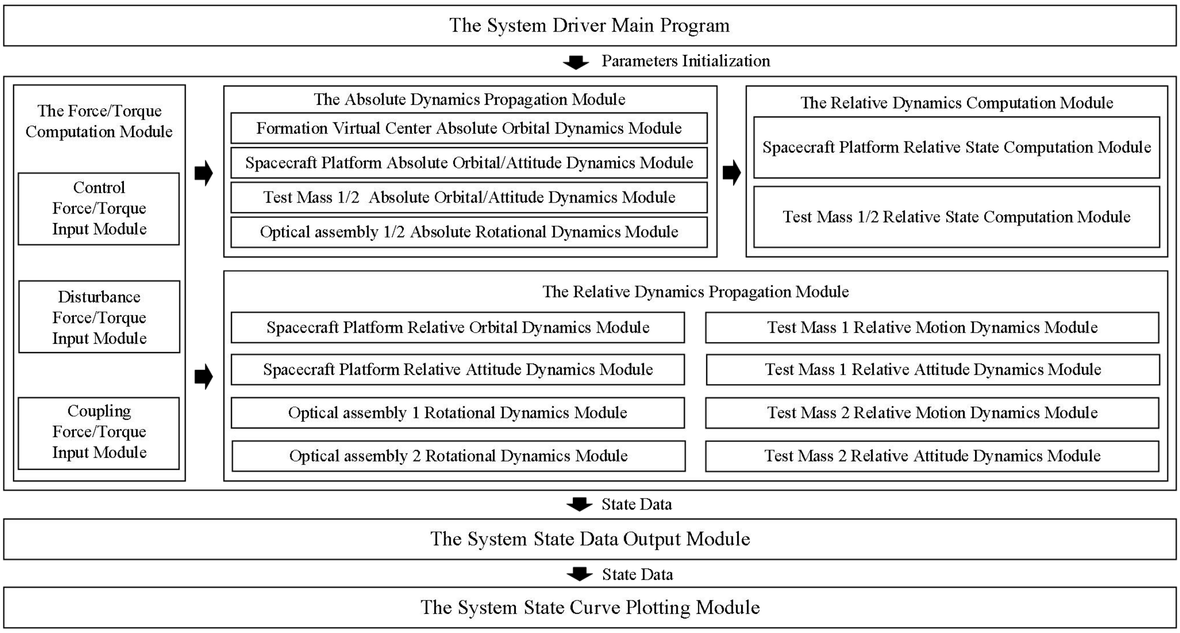

Fig. 2 The composition of the dynamic simulation system of DFACS

(3) The Absolute Dynamics Propagation Module conducts numerical integration of the spacecraft and test masses' absolute orbital dynamics, based on a two-body model with perturbative forces. It outputs inertial states, including position, velocity, attitude angles, and angular acceleration.

(4) The Relative Dynamics Computation Module derives the relative states of the spacecraft, test masses, and optical assemblies by processing inertial states through non-differential operations. This module is distinct from the subsequent Relative Dynamics Propagation Module, which employs differential equations.

(5) The Relative Dynamics Propagation Module computes the relative states of the spacecraft, test masses, and optical assemblies using differential equations with force and torque inputs. This contrasts with the relative dynamics computation module, which derives relative states from absolute states without integration.

(6) The System State Data Output Module consolidates and outputs data computed by various dynamic modules.

(7) The System State Curve Plotting Module generates graphical representations of the system dynamics, including the inertial states of the formation’s virtual center and spacecraft (orbital and attitude), the spacecraft’s relative states with respect to the formation virtual center, the inertial and relative states of test masses 1 and 2, and the rotational states of optical assemblies 1 and 2 (angles and angular velocities).

ISSN:3007-9640 DOI: https://doi.org/10.70114/acmsr.2025.2.1.P240

Each module plays a specific role in achieving the system's comprehensive functionality, ensuring accurate dynamic modeling and simulation.

4.2 The Validation of DFACS Nonlinear Dynamics Model

In Section 3, a set of differential equations is formulated using the relative state variables of the spacecraft $\boldsymbol{r}_{\mathrm{S}}$, $\boldsymbol{q}_{\mathrm{S}}$, the test mass $\boldsymbol{r}_{\mathrm{M}}$, $\boldsymbol{q}_{\mathrm{M}}$, and the telescope rotation angle ζ. To verify the accuracy of the proposed nonlinear model, it is necessary to validate the correctness of these differential equations. Leveraging the authoritative nature of absolute orbital dynamics, two approaches are employed to compute the DFACS relative state: 1) direct computation using the proposed relative state differential equations. 2) computation based on inertial state differential equations, followed by a non-differential transformation to derive the relative state. A comparison of the results obtained from these two methods demonstrates that a small discrepancy between them confirms the validity of the proposed model.To implement this validation framework, a verification system depicted in Fig. 3 was developed on the Simulink platform, based on the simulation system shown in Fig. 2. Approach 1, corresponding to the relative dynamics propagation module, directly computes the relative states of DFACS. Apporach 2 indirectly computes the relative states by first solving for the inertial states and subsequently deriving the relative states. The comparison of the results from these two paths allows for verifying the accuracy of the proposed model.

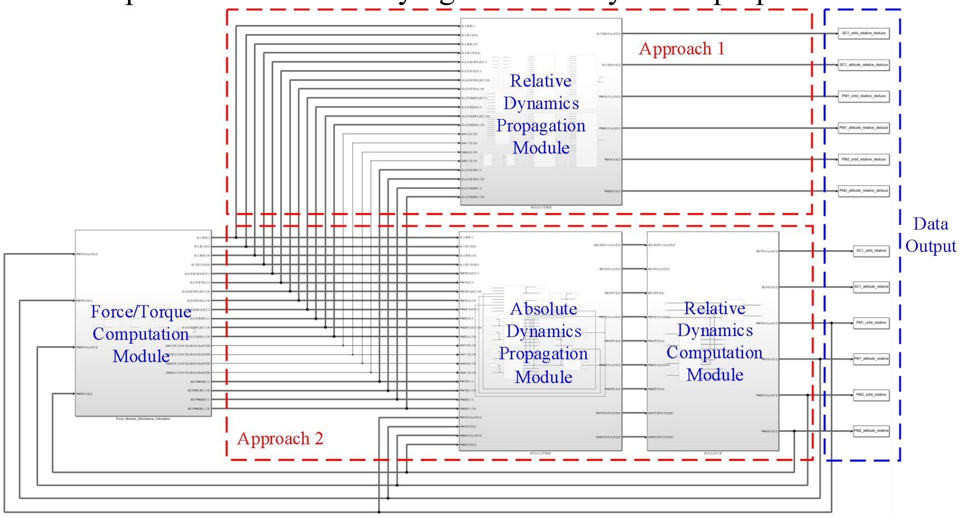

Fig. 3 The composition of the dynamic simulation system of DFACS

For space gravitational wave detection missions, drag-free control aims to minimize residual acceleration in the test mass's sensitive degrees of freedom. Thus, the test mass's relative motion state with respect to the ORF is critical for DFACS. This subsection evaluates the DFACS model's correctness using the test mass's relative position $\boldsymbol{r}_{\mathrm{S}}$ and velocity $\dot{\boldsymbol{r}}_{\mathrm{S}}$ as key states. It also examines the effects of integration methods, step sizes, and times. Four simulation cases, detailed in Table 1, are designed for this analysis.

Table 1. Different integrator parameter settings for simulation

Case	Integration method	Step	Time
Case 1	Runge-Kutta	1000 s	1 year
Case 2		5000 s	
Case 3		10000 s	
Case 4	Dormand-Prince	Auto	
Case 5			1 day

ISSN:3007-9640 DOI: https://doi.org/10.70114/acmsr.2025.2.1.P240

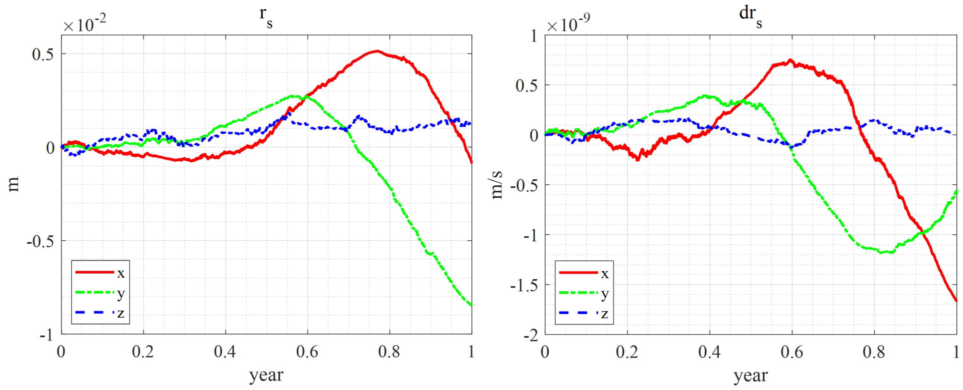

Fig. 4 The simulation result of case 1

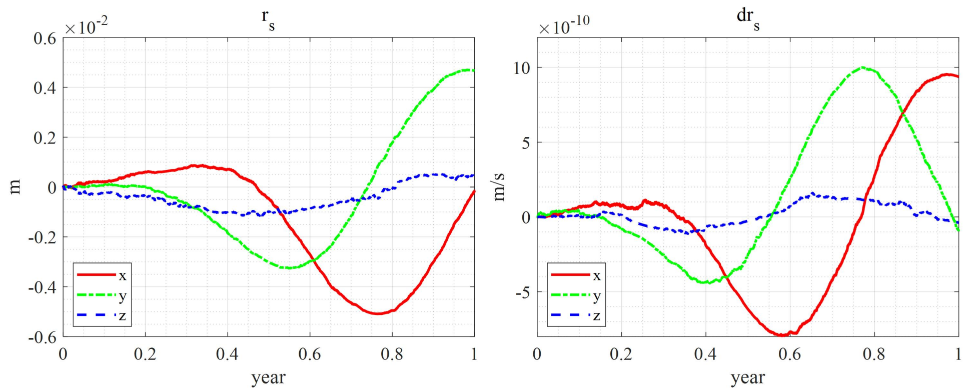

Fig. 5 The simulation result of case 2

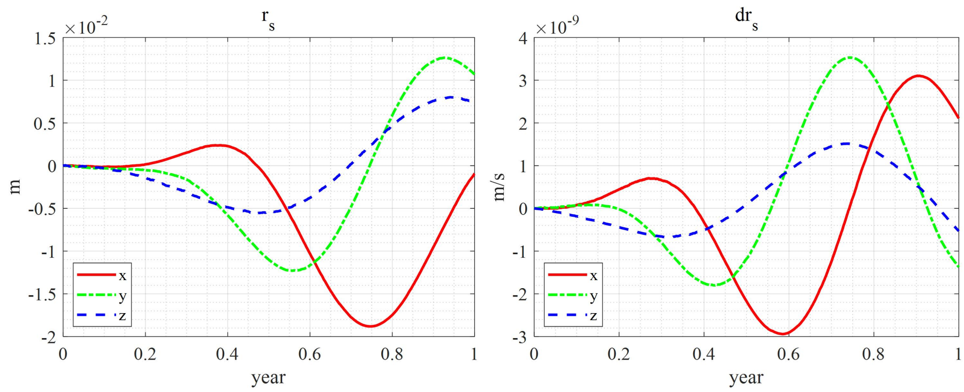

Fig. 6 The simulation result of case 3

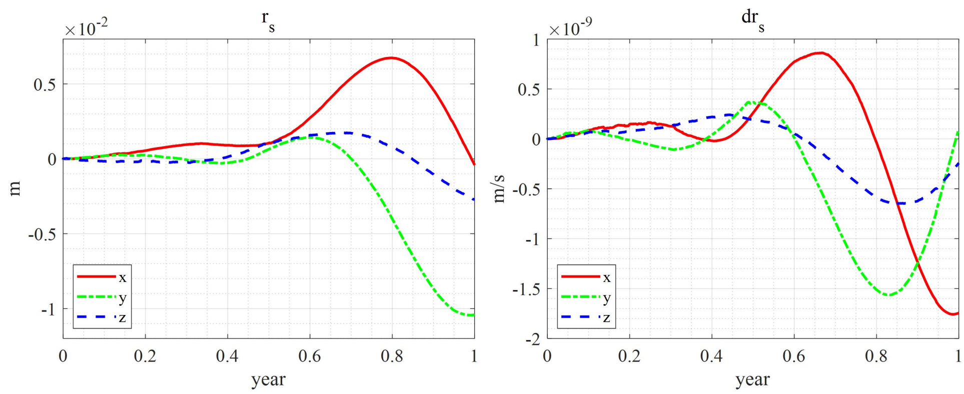

Fig. 7 The simulation result of case 4

ISSN:3007-9640 DOI: https://doi.org/10.70114/acmsr.2025.2.1.P240

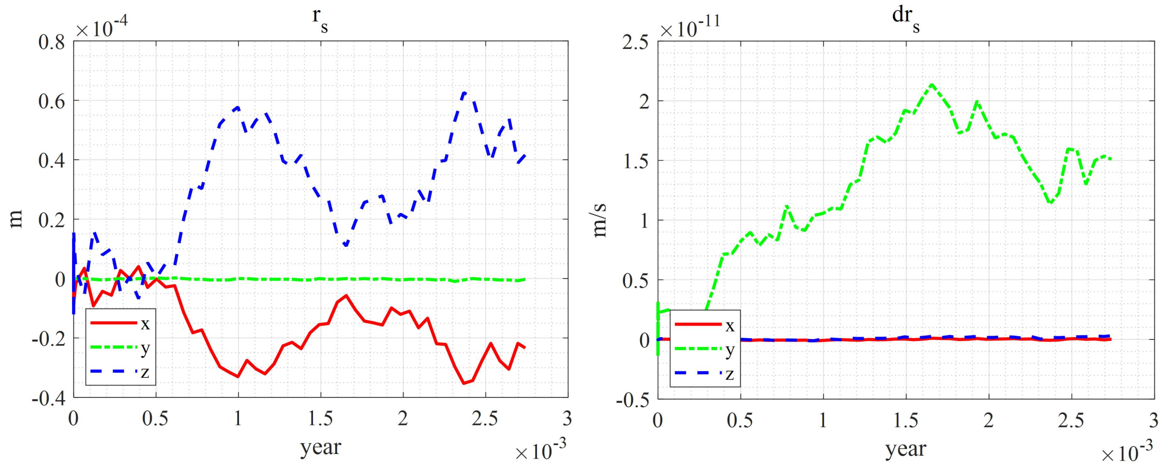

Fig. 8 The simulation result of case 5

Table 2. Max error in relative position and relative velocity under different cases

Case	Max error of relative position	Max error of relative velocity
Case 1	8.477×10^{-3} m	1.670×10^{-9} m/s
Case 2	5.089×10^{-3} m	1.000×10^{-9} m/s
Case 3	1.881×10^{-2} m	3.529×10^{-9} m/s
Case 4	1.044×10^{-2} m	1.758×10^{-9} m/s
Case 5	6.258×10^{-5} m	2.1377×10^{-11} m/s

Fig. 4 to Fig. 8 illustrate the error variation curves of the relative position and relative velocity of the test mass with respect to ORF under five different scenarios, calculated using two computational paths. Table 2 presents the maximum errors in relative position and relative velocity for these five cases.

First, examining cases 1 to 4, we observe the order of magnitude of the relative position and relative velocity errors. The maximum error in relative position is concentrated around the 10^{-2} order of magnitude, while the maximum error in relative velocity is concentrated around the 10^{-9} order of magnitude. The integration time is on the order of 10^{7}. It can be seen that the error in relative velocity accumulates into the error in relative position, leading to the further inference that the maximum error in relative acceleration should be on the order of 10^{-16}, which validates the correctness of the model established in this paper (the same conclusion applies to case 5).

Secondly, theoretically, the results calculated by the two paths shown in Figure 8 should have no error. However, based on the results in Fig. 4 to Fig. 7, some discrepancies are observed between the two calculation paths. The reason for this is the difference in error propagation paths during the integration process (for example, the error generated after the integration in path 2 must pass through the "Relative Dynamics Computation Module"). This discrepancy is also evident in the integration time; for cases 4 and 5, as the integration time increases, this discrepancy is amplified.

In summary, the calculation errors between the two paths are not inherent errors arising from model correctness but are instead cumulative integration errors due to differences in error propagation paths. Therefore, these errors do not affect the judgment of the model's correctness. Finally, based on the comparison in Table 2, different integration methods and step sizes are considered. For the fixed-step Runge-Kutta method, the error does not show a strict positive correlation with step size. Additionally, compared to the variable-step Dormand-Prince method, the Runge-Kutta method does not demonstrate a significant advantage in terms of error, while the Dormand-Prince method offers higher computational efficiency.

ISSN:3007-9640 DOI: https://doi.org/10.70114/acmsr.2025.2.1.P240

5. Summary

This paper focuses on the nonlinear dynamic modeling of DFACS with two test masses for the heliocentric space gravitational wave detection mission, addressing the challenge of coupled dynamics in complex space environments. The study begins by clarifying DFACS components and modeling assumptions, then constructs a dynamic model covering all system elements. Key coordinate systems are defined, and an innovative formation coordinate system is proposed to improve clarity and computational efficiency in describing formation dynamics. A comprehensive nonlinear dynamic model is developed, including spacecraft dynamics, test mass dynamics, optical assembly rotation, and coupled force model between the spacecraft and test masses. A nonlinear dynamic simulation system is created to verify the model's accuracy, demonstrating its potential applications in control design and performance evaluation. The results provide a systematic methodology for DFACS modeling and lay the foundation for future research in control design, state estimation, and related areas. Despite the thorough analysis, further optimization is possible, including the development of high-precision nonlinear model linearization techniques and refined environmental disturbance models to improve system adaptability. Future research should focus on high-precision computational methods to meet the computational and accuracy requirements of gravitational wave detection.

Acknowledgements

This research was supported by National Key R&D Program of China: Gravitational Wa ve Detection Project (No.2021YFC22026, No.2021YFC2202601, No.2021YFC2202603, No.20 24YFC2207900) and National Natural Science Foundation of China (No.12172288 and No.1 2472046).

References

[1] Wu Z, Hu Y M, Fan H M, et al. Searching for gravitational-wave bursts with space-borne detectors[J]. Physical Review D, 2024, 109(10): 103004.

[2] Armano M, Audley H, Baird J, et al. In-depth analysis of LISA Pathfinder performance results: Time evolution, noise projection, physical models, and implications for LISA[J]. Physical Review D, 2024, 110(4): 042004.

[3] Chen Z C, Huang Q G, Liu C, et al. Prospects for Taiji to detect a gravitational-wave background from cosmic strings[J]. Journal of Cosmology and Astroparticle Physics, 2024, 2024(03): 022.

[4] An Z, Shao K, Gu D, et al. Analysis and comparison of the orbit determination accuracy of TianQin based on multiple ground-based measurements[J]. Physica Scripta, 2024, 99(8): 085003.

[5] Jiao B H, Liu Q F, Dang Z H, et al. A review on DFACS (I): System design and dynamics modeling[J]. Chinese Journal of Aeronautics, 2024, 37(5):92-119.

[6] Liao H , Xu Y , Zhu Z ,et al.A new design of drag-free and attitude control based on non-contact satellite[J].ISA transactions, 2019, 88:62-72.

[7] Liu S , Liao H , Xie J ,et al.A non-contact spacecraft architecture with extended stochastic state observer based control for gravity mission[J].Journal of Systems Engineering and Electronics, 2021, 32(2):460-472.

[8] Dang Z H. Modeling and controller design of inner-formation flying system with two proof-masses[J]. Aerospace Science and Technology, 2013, 30(1): 8-17.

[9] Ma H, Han P, Gao D, et al. H_∞ robust controller design for deep space drag-free satellite with two test masses[J]. J. Harbin Inst. Technol, 2021, 53(2): 1-13.

[10] Canuto E, Molano-Jimenez A, Perez-Montenegro C, et al. Long-distance, drag-free, low-thrust, LEO formation control for Earth gravity monitoring[J]. Acta Astronautica, 2011, 69(7-8): 571-582.

[11] Xiao C, Canuto E, Hong W, et al. Drag-free design based on embedded model control for TianQin project[J]. Acta Astronautica, 2022, 198: 482-494.

ISSN:3007-9640 DOI: https://doi.org/10.70114/acmsr.2025.2.1.P240
[12] Liu P, Dang Z. Triangular formation dynamics and optimal control for space-based gravitational-wave observatory[J]. Journal of Command and Control, 2021, 7(3): 275-286.

[13] Ploen S, Quadrelli M, Scharf D, et al. Dynamics of drag-free formations for earth imaging applications. Reston: AIAA; 2006. Reprot No.:AIAA-2006-6016 .

[14] Vidano S, Novara C, Colangelo L, et al. The LISA DFACS: A nonlinear model for the spacecraft dynamics[J]. Aerospace Science and Technology, 2020, 107: 106313.